

# Time-resolved cathodoluminescence study of carrier relaxation, transfer, collection, and filling in coupled $\text{In}_x\text{Ga}_{1-x}\text{N}/\text{GaN}$ multiple and single quantum wells

S. Khatsevich and D. H. Rich

Department of Physics, Ilse Katz Center for Meso and Nanoscale Science and Technology, Ben-Gurion University of the Negev, P.O. Box 653, Beer-Sheva 84105, Israel

S. Keller and S. P. DenBaars

Electrical and Computer Engineering and Materials Departments, University of California, Santa Barbara, California 93111, USA

(Received 22 August 2006; revised manuscript received 20 October 2006; published 17 January 2007)

We have examined in detail the optical properties and carrier capture dynamics of coupled  $\text{In}_x\text{Ga}_{1-x}\text{N}/\text{GaN}$  multiple and single quantum well (MQW and SQW) structures that possess various numbers of QWs in the confinement region adjacent to a SQW. The aim is to study the influence of the structure of an InGaN MQW confinement region on carrier transfer and collection into a coupled SQW. By applying in a complementary way temperature- and excitation-dependent cathodoluminescence (CL) spectroscopy and time-resolved CL measurements, we have analyzed the carrier dynamics and state filling in the SQW and the adjacent MQW. We solved self-consistently the nonlinear Poisson-Schrödinger equation for wurtzite materials including strain, deformation potentials, and piezoelectric field of our  $\text{In}_x\text{Ga}_{1-x}\text{N}/\text{GaN}$  single and multiple QW structures to obtain the excitation-dependent eigenstates that are used to calculate band filling, excitonic lifetimes, and exciton binding energies. We show that it is possible to treat a coupled  $\text{In}_x\text{Ga}_{1-x}\text{N}$  single and multiple QW system in a way that allows for a determination of the quasi-Fermi levels, carrier densities in separated QWs, luminescence efficiencies, thermal activation energies for carrier transfer, and carrier capture and recombination rates. We demonstrate in this unique method an improved determination of the piezoelectric field and In composition  $x$  by a *non-contact* optical means alone. The results demonstrate an enhanced luminescence efficiency and yet decreased carrier capture rate by the SQW as the number of QWs increases in the adjacent MQW confinement region.

DOI: [10.1103/PhysRevB.75.035324](https://doi.org/10.1103/PhysRevB.75.035324)

PACS number(s): 78.30.Fs, 78.67.De, 78.60.Hk

## I. INTRODUCTION

In recent years, much attention has been paid to a new class of low-dimensional structures, made of hexagonal (wurtzite) group III nitride semiconductors.  $\text{In}_x\text{Ga}_{1-x}\text{N}/\text{GaN}$  single quantum wells (SQWs) and multiple quantum wells (MQWs) have been studied intensively both experimentally and theoretically due to their potential applications for the production of efficient optoelectronic devices, such as light-emitting diodes<sup>1,2</sup> and laser diodes<sup>3</sup> that can emit in the blue/violet spectral region. Despite the enormous progress in the material growth and device fabrication of III-V nitrides in the past years, the physical processes responsible for the bright light emission in InGaN MQW structures are not completely understood due to a complex alloy phase separation,<sup>4-6</sup> a high threading dislocation density ( $10^8-10^{10}\text{ cm}^{-2}$ ),<sup>7</sup> and large-strain-induced piezoelectric<sup>8-10</sup> and spontaneous<sup>9,10</sup> polarizations, which lead to large electric fields in the strained layers. Many studies have reported the important role of the large internal electric field in InGaN QWs,<sup>9</sup> comparable to or much larger than  $\sim 1\text{ MV/cm}$ , which induces a large redshift in the transition energies,<sup>11,12</sup> due to the quantum confined Stark shift effect (QCSE),<sup>12-14</sup> and attendant reduction in the oscillator strength,<sup>12,14,15</sup> owing to the field-induced separation of the electron and hole wave functions toward the opposite sides of the QW. A thorough understanding of the optical properties of  $\text{In}_x\text{Ga}_{1-x}\text{N}/\text{GaN}$  MQWs at different temperatures and excitations is of particular importance for the design of group III-nitride light-emitting devices. A number of different ef-

fects, causing a blue-shift of the emission spectrum, were predicted and experimentally verified at high-excitation densities, such as carrier-induced screening of the internal electric field in the well,<sup>16-19</sup> screening of the excitonic interaction at carrier densities larger than the Mott density,<sup>20</sup> and band-filling effects.<sup>18,19,21</sup>

Since most QW-based devices are intended to work at room temperature (RT), an understanding of their behavior at high temperatures is of great importance. Although operation of such devices has been demonstrated at RT,<sup>22</sup> it is desirable to improve and optimize their luminescence efficiency which is affected by different nonradiative processes, such as carrier thermal escape from QWs and capture of carriers at defects and threading dislocations.<sup>23</sup> Such nonradiative processes may become dominant when the temperature of the sample is raised to 300 K.<sup>24,25</sup> As was shown recently, the design of the confinement region adjacent to the InGaN SQWs can significantly improve their luminescence efficiency at RT.<sup>26</sup> The enhanced luminescence efficiency of the SQWs was attributed to the high efficiency of carrier transfer from MQWs that were placed in a confinement region adjacent to the SQW.<sup>26</sup> Yet, to our knowledge, no detailed studies exist concerning the influence of the MQW structural details in the confinement region on the carrier capture and subsequent luminescence efficiency of the InGaN SQWs. From a fundamental perspective, it would be useful to construct a detailed experimental and theoretical analysis of a variety of selectively positioned InGaN QWs (or the judicious placement of an InGaN MQW) in confining layers adjacent to a typical optically active InGaN SQW such that the MQW and

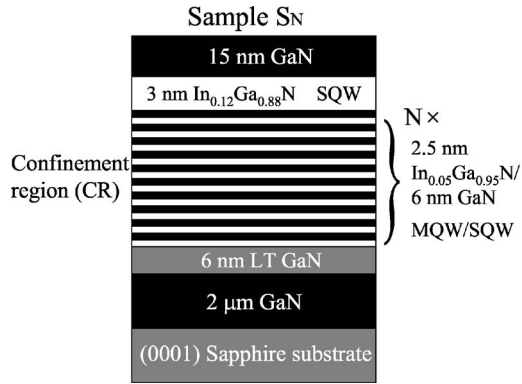


FIG. 1. Schematic diagram of the InGaN MQW and SQW samples.  $S_N$  refers to the particular sample number ( $N=1, 2, 4, \text{ or } 8$ ).  $N$  also refers to the number of nominal  $\text{In}_{0.05}\text{Ga}_{0.95}\text{N}$  QWs in the MQW. SQW region contains a single nominal  $\text{In}_{0.12}\text{Ga}_{0.88}\text{N}$  single QW for all samples.

SQW are electronically coupled. The aim will be to systematically examine how such QWs in the confinement region can influence the carrier relaxation, assist carrier collection and transfer to the InGaN SQW of interest, and affect the efficiency of excitonic luminescence in the SQW.

In this paper we report on a detailed study of the luminescence properties of samples containing 3 nm thick InGaN SQWs possessing different numbers of QWs in the MQW confinement region. We studied the carrier capture dynamics, coupling, and transfer between the SQW and MQW of the confinement region. The MQWs provide a set of optical markers which exhibit key signatures in the wavelength and time domain that help visualize the carrier relaxation, capture, and transfer into the SQW. We employed, in a complementary way, temperature- and excitation-dependent cathodoluminescence (CL) spectroscopy, and time-resolved CL measurements of onset and decay rates. Our experimental results were further modeled by calculating the QW energy states and wave functions for various excitation densities and temperatures. In performing these calculations, we solved the Schrödinger and Poisson equations self-consistently, within a single band effective mass approximation. We developed an excitation-dependent luminescence model that enables a determination of quasi-Fermi levels, carrier densities, carrier capture and recombination rates, and quantum efficiency of luminescence in the coupled MQW and SQW system and applied it to our experimental results. We further determined to an improved accuracy, beyond that estimated from sample growth conditions, values of the In composition  $x$  and the piezoelectric field in QWs of the confinement region and in the SQW.

## II. EXPERIMENTAL DETAILS

The InGaN MQW samples were grown on  $c$ -plane sapphire by metal-organic chemical-vapor deposition (MOCVD) using trimethylgallium, trimethylindium, disilane and ammonia as precursors, as has been described previously.<sup>26</sup> Four InGaN MQW samples were grown. A schematic diagram of their structure is shown in Fig. 1. First,

the 2  $\mu\text{m}$  thick GaN:Si buffer layer was grown on  $c$ -plane sapphire substrate at 1060  $^\circ\text{C}$ , followed by deposition of 6 nm low-temperature (LT) GaN layer. The confinement region (CR), the 3 nm thick  $\text{In}_x\text{Ga}_{1-x}\text{N}$  SQW with  $x \approx 0.12$ , nominally, and the 15 nm thick GaN capping layer (see Fig. 1) were grown at 800  $^\circ\text{C}$ . In sample S1, a 25 nm thick  $\text{In}_y\text{Ga}_{1-y}\text{N}$ , 6 nm thick GaN confinement layer with low nominal indium composition  $y \approx 0.05$  was deposited in the confinement region prior to growth of the  $\text{In}_{0.12}\text{Ga}_{0.88}\text{N}$  SQW. In the other three samples (labeled as S2, S4, and S8), 2, 4, and 8 periods of a 2.5 nm thick  $\text{In}_{0.05}\text{Ga}_{0.95}\text{N}$ , 6-nm-thick GaN layer were deposited prior to the SQW, respectively, as illustrated schematically in Fig. 1.

The cathodoluminescence (CL) experiments were performed with a modified JEOL-5910 scanning electron microscope using a 15 keV electron beam with probe current in the 0.03 to 40 nA range.<sup>27</sup> A UV multialkali photomultiplier tube operating in the 185 to 850 nm spectral range enabled photon counting of the luminescence that was dispersed by a 0.25 m monochromator. Measurements were performed at different temperatures in the 50 to 310 K temperature range. In order to increase the range of accessible excitation densities, the excitation volume was varied by defocusing the electron beam in reproducible steps as has been described in detail elsewhere.<sup>28,29</sup> In the very low-excitation density regime, the electron beam was defocused to a spot with a diameter of  $\sim 90 \mu\text{m}$  at the sample surface. The defocusing approach permits measuring CL emission with a uniform excitation density that is several orders of magnitude smaller than what can be employed using a focused electron beam.<sup>29</sup> Time-resolved CL experiments were performed with the method of delayed coincidence in an inverted single-photon counting mode, with a time resolution of  $\sim 100 \text{ ps}$ .<sup>27,30</sup> Electron beam pulses of 50 ns width with a 1 MHz repetition rate were used to excite the sample. Steady-state and time-delayed CL spectroscopy measurements were performed with a spectral resolution of 1 nm. The latter was used to obtain spectrally integrated intensities for selected features of the CL spectra in various time domains.<sup>27</sup>

## III. RESULTS AND DISCUSSIONS

### A. Cathodoluminescence (CL) spectroscopy at different temperatures and excitations

Figure 2 shows spatially integrated CL spectra of samples S1–S8 acquired while the focused electron beam ( $I_b = 400 \text{ pA}$ ) was rastered over a  $64 \mu\text{m} \times 48 \mu\text{m}$  region at low and high temperatures. All spectra are normalized to have nearly the same intensity; the scaling factors are indicated. Various peaks are identified as the near-band edge GaN emission, emission that stems from the shallow quantum wells in the confinement region (CR), and the SQW emission, as labeled in Fig. 2. At high temperatures, emission is dominated by the SQW emission, as seen in Fig. 2(a). This is consistent with previous results for samples possessing similar structures.<sup>26</sup> At low temperatures all samples emit predominantly from the confinement region, with a much weaker emission that stems from the SQW, as seen in Fig. 2(b). It is important to note that for an e-beam energy of

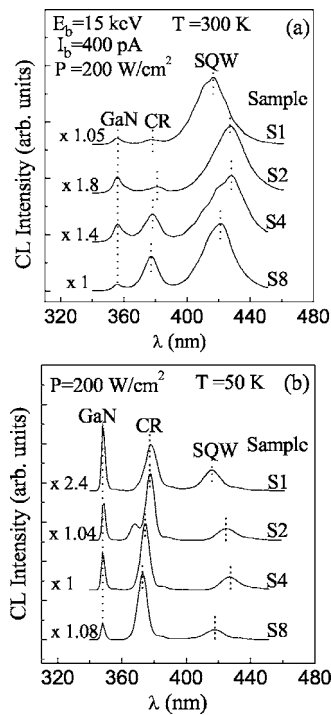


FIG. 2. Spatially integrated and constant excitation CL spectra of samples S1–S8 acquired at high-excitation density,  $P = 200 \text{ W/cm}^2$ , for (a)  $T = 300 \text{ K}$  and (b)  $T = 50 \text{ K}$ . The SQW and the CR emission peaks are indicated in each sample by vertical dashed lines.

15 keV, about 95% of the electron-hole pairs are created deep in the GaN buffer layer, below the confinement region. It is therefore natural to assume that initial carrier capture from the GaN buffer layer into the CR is followed by carrier transfer from the CR into the SQW. A semi-log plot of the spatially and spectrally integrated CL intensities of the SQW and CR emission acquired under high constant excitation condition ( $I_b = 400 \text{ pA}$ ) vs temperature is shown in Fig. 3 for sample S1, and similar results were obtained for samples S2–S8. The increase in the integrated CL intensity of the SQW emission at temperatures above 120 K is correlated with the observed decrease in the integrated CL intensity of the CR emission. This is likely caused by a thermally activated carrier transfer from the QWs of the CR into the SQW, as seen in Fig. 3. The inset of Fig. 3 shows a semi-logarithmic plot of the integrated CL intensities of the CR emission for samples S1–S8 vs  $1/k_B T$  under high-excitation condition, which exhibits an Arrhenius behavior. The solid lines indicate the results of linear fits of the log of intensity vs  $1/k_B T$  data in the 200 to 300 K temperature range, from which corresponding activation energies are determined. A similar behavior is observed for samples S2–S8 with activation energies in the 130–136 meV range at high temperatures. Sample S1 shows a markedly different behavior with much lower activation energy of  $\sim 60 \text{ meV}$  in the 200 to 300 K temperature range, as indicated in Fig. 3.

Spatially and spectrally integrated CL intensities of the SQW emission acquired with a focused and strongly defocused electron beam (under constant excitation) in the  $50 \leq T \leq 310 \text{ K}$  temperature range are shown in Fig. 4 for

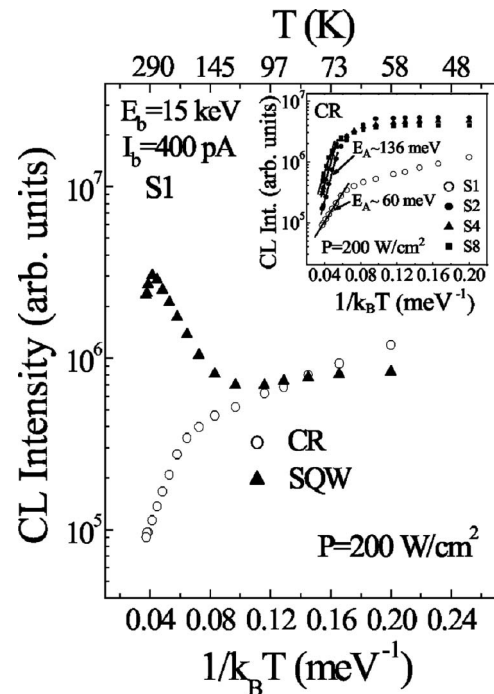


FIG. 3. A semi-logarithmic plot of the spatially and spectrally integrated CL intensities of the SQW and CR emission vs  $1/k_B T$  acquired under high constant excitation condition,  $P = 200 \text{ W/cm}^2$ , for sample S1. The inset shows a semi-log plot of the integrated CL intensities of the CR emission for samples S1–S8 vs  $1/k_B T$  under a high-excitation condition,  $P = 200 \text{ W/cm}^2$ , which exhibit an Arrhenius behavior. The solid lines indicate the results of linear fits in the temperature range of 200–300 K, from which corresponding activation energies are determined from the slopes, as shown.

samples S1–S8. The relationship between the excitation density  $P$  and probe current  $I_b$  can be approximated by

$$P \approx \frac{I_b E_b}{e S_e}, \quad (1)$$

where  $E_b$  is the e-beam energy (15 keV),  $S_e$  is the excitation area, which is  $3 \mu\text{m}^2$  and  $6300 \mu\text{m}^2$  for focused and defocused electron beams, respectively. For  $I_b = 400 \text{ pA}$ , this yields an excitation density of  $200 \text{ W/cm}^2$  and  $95 \text{ mW/cm}^2$  for focused and strongly defocused e-beams, respectively. The specific onset temperatures  $T_{\text{ON}}$  that are associated with an increase in the CL intensity of the SQW emission are indicated in each sample for low- and high-excitation densities, as shown in Fig. 4 with arrows. A lower  $T_{\text{ON}}$  and a more rapid increase in the integrated CL intensity of the SQW emission with increasing temperature are observed for the case of high-excitation density in all samples, as seen in Fig. 4. State filling of the QWs in the CR and saturation of non-radiative recombination channels in the SQW are responsible for this temperature- and excitation-dependent behavior, as will be shown more completely in Sec. V. Nearly identical onset temperatures of  $\sim 180 \text{ K}$  (200 K) are obtained for the three samples S2, S4, and S8 under high- (low-) excitation densities. A lower onset temperature of  $\sim 120 \text{ K}$  (140 K), observed for sample S1 at high (low) excitation, is correlated

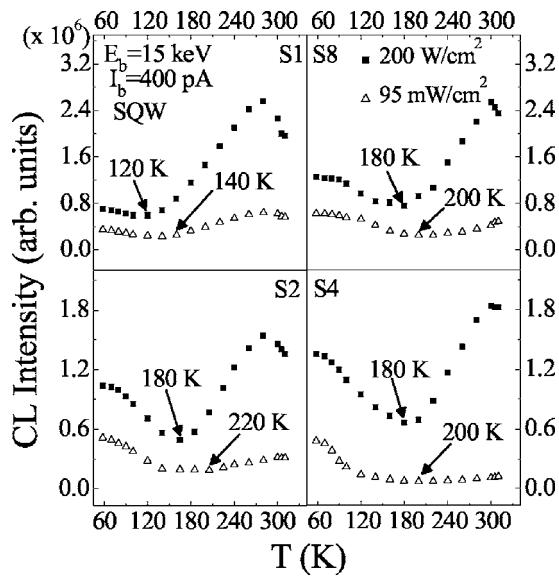


FIG. 4. Spatially and spectrally integrated CL intensities of the SQW emission acquired under high and low constant excitation conditions in the  $50 \leq T \leq 310$  K temperature range for samples S1–S8. Temperatures associated with the onset of the increase in the CL intensity  $T_{ON}$  are indicated with arrows in each sample at low and high excitations.

with the lower activation energy of the CR emission that was measured for that sample, as shown in the inset of Fig. 3.

The SQW peak energies, as determined by Gaussian fits, vs temperature under a high-excitation condition are shown in Fig. 5 for samples S1–S8. The behavior of the SQW peak energy vs  $T$  for sample S1 exhibits an *S-shaped* temperature dependence of the QW peak energy that was observed in previous studies of InGaN MQW materials and is attributed to carrier localization in QWs at low temperatures.<sup>31–35</sup> The S-shaped temperature dependence observed for sample S1 strongly suggests that exciton localization plays a dominant role for this sample at temperatures below 120 K. In samples S2–S8, the SQW peak energy does not vary much at low

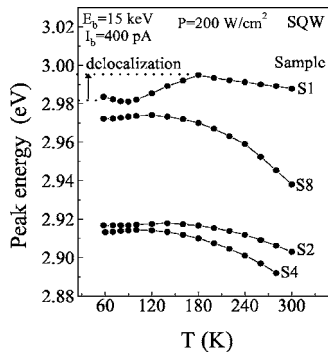


FIG. 5. The temperature dependence of the SQW peak energy position, extracted by Gaussian fit for samples S1–S8 under high-excitation condition,  $P=200$  W/cm<sup>2</sup>. For sample S1, an increase in the peak energy at low temperatures indicates that excitons are trapped at small potential minima and exhibit the classical S-shaped energy dependence. The temperature range for such localization is indicated by horizontal dotted lines.

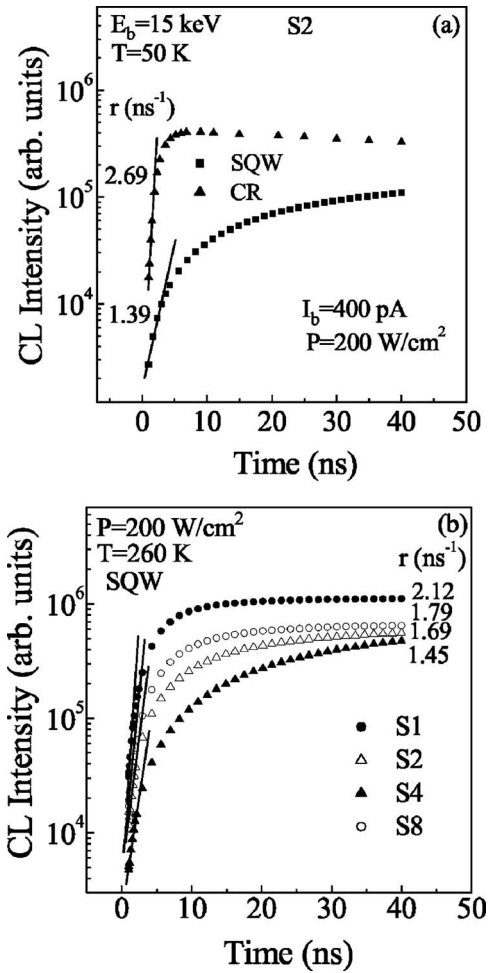


FIG. 6. A semi-logarithmic plot of the spatially and spectrally integrated CL intensities vs onset time for (a) the SQW and CR emission for sample S2 at  $T=50$  K and (b) the SQW emission for samples S1–S8 at  $T=260$  K. A high-excitation density,  $P=200$  W/cm<sup>2</sup>, was used. The results are shown for various onset times ranging from 250 ps to 40 ns. Initial onset rates  $r$  obtained by a linear fit from the slopes of the onset curves are indicated for each sample.

temperatures and shifts to the red for temperatures above 120 K. This behavior indicates that the SQW emission in these samples results likely from recombination of free excitons.<sup>33</sup> An identification of the type of localization for each sample is essential, as this will be used in an analysis of calculated radiative lifetime in Sec. V.

### B. Time-resolved CL measurements

Integrated CL intensities of the total CR and SQW emissions, obtained under a high-excitation condition,  $P=200$  W/cm<sup>2</sup>, from time-delayed spectra of sample S2, are shown in a log of CL intensity vs time plot in Fig. 6(a) for various onset times from 250 ps to 40 ns at  $T=50$  K. An initial rapid increase in the integrated CL intensity of the CR emission, for about 5 ns, is followed by a slow decrease that is correlated with an increase in the integrated CL intensity of the SQW emission, indicating carrier funneling from the

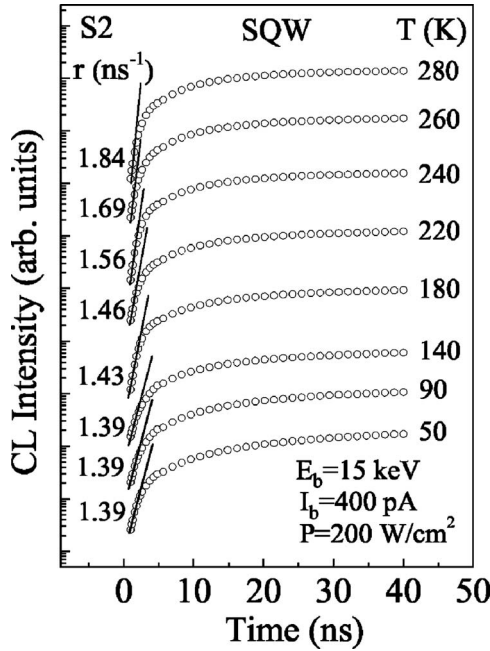


FIG. 7. A semi-logarithmic plot of the spatially and spectrally integrated CL intensities of the SQW emission for sample S2 shown for various onset times and temperatures in the  $50 \leq T \leq 280$  K range at high-excitation density,  $P=200$  W/cm<sup>2</sup>. Initial onset rates  $r$  obtained by a linear fit from the slopes of the onset curves are indicated at each temperature. The initial onset rate of the SQW emission is found to be independent of temperature for  $T < \sim 100$  K, strongly suggesting that carrier tunneling from the ground-state levels of QWs in the confinement region (CR) enables carrier transfer into the SQW at low temperatures.

CR to the SQW. In order to quantify the initial increase in the CL intensity with time, the onset rates,  $r = \Delta \ln(I_{CL}) / \Delta t$ , given by the slopes of the tangents to the onset curves, are defined as shown in Figs. 6 and 7 for the onset part of the CL transients. The initial onset rates measured at  $T=50$  K and high excitation,  $P=200$  W/cm<sup>2</sup>, for sample S2 are 1.39 and 2.69 ns<sup>-1</sup> for the SQW and CR emission, respectively, as seen in Fig. 6(a). This is also consistent with the observation that carrier transfer from QWs of the CR into the SQW is responsible for the observed slow rise of the SQW peak at low temperatures. Integrated CL intensities of the SQW emission, obtained under a high-excitation condition,  $P=200$  W/cm<sup>2</sup>, from time-delayed spectra measurements of samples S1–S8 are shown in a log of CL intensity vs time plot in Fig. 6(b) for various onset times from 250 ps to 40 ns at  $T=260$  K. The initial onset rates of the SQW emission measured at  $T=260$  K and high excitation,  $P=200$  W/cm<sup>2</sup>, are 2.12, 1.69, 1.45, and 1.79 ns<sup>-1</sup>, respectively, for samples S1–S8, as shown in Fig. 6(b). The highest initial onset rate of the SQW emission and the most efficient luminescence at high temperatures is observed for sample S1, with a thick QW in the CR, and for sample S8, with MQW confinement layers, as seen from Figs. 2(a), 4, and 6(b). These two samples also have the highest total luminescence efficiency at RT, as will be shown later in this section. Spatially and spectrally integrated CL intensities of the SQW emission of sample S2 with  $P=200$  W/cm<sup>2</sup> are shown in Fig. 7 for vari-

ous onset times in the  $50 \leq T \leq 280$  K temperature range. The increase in the initial onset rate of the SQW emission with an increase in temperature for  $T > \sim 180$  K indicates that at high temperatures the carrier capture into the SQW is a thermally activated process. At temperatures below  $\sim 100$  K, the initial onset rate,  $r=1.39$  ns<sup>-1</sup>, of the SQW emission is temperature independent, suggesting that carrier tunneling from the ground-state levels in QWs of the CR is most likely the dominant process responsible for the carrier transfer into the SQW. Similar results were obtained for samples S4 and S8, whereas sample S1 showed a temperature-dependent behavior down to 50 K, indicating an incomplete saturation for this sample.

We recall that the measured decay lifetime  $\tau$  at temperature  $T$  is related to the radiative and nonradiative recombination times  $\tau_R$  and  $\tau_{NR}$ , respectively, by  $\tau^{-1} = \tau_R^{-1} + \tau_{NR}^{-1}$ . The radiative lifetime increases as temperature increases while the tendency of the nonradiative lifetime is the opposite. In order to determine the predominant recombination process at temperatures close to 50 K, decay lifetimes of the SQW and CR peak emissions were measured at different temperatures and excitations. The CL intensity vs time transients of the SQW peak emission acquired for sample S2 at high-excitation density,  $P=200$  W/cm<sup>2</sup>, are shown in Fig. 8(a) for various different sample temperatures in the  $50 \leq T \leq 280$  K range. Initial luminescence decay times measured from the slopes of the semi-log plots are indicated at different temperatures, as shown. From Fig. 8(a),  $\tau$  decreases from 30.3 to 10 ns, as  $T$  increases from 50 to 280 K. A rapid decrease in the decay lifetimes for  $T \geq 70$  K indicates the important role of nonradiative processes at higher temperatures. At low temperatures and high excitation, a nonexponential decay due to a screening of electric fields is observed, in which the decay time  $\tau$ , which is measured from the slopes in the decay curve, increases with time.<sup>17–19</sup> An opposite behavior is observed at high temperatures and high excitation, in which the CL transient starts with a slow decay and becomes faster. Such behavior was previously observed in isolated (uncoupled) In<sub>x</sub>Ga<sub>1-x</sub>N/GaN QWs and was explained through a suppression of nonradiative recombination channels by a saturation of defects with carriers.<sup>25</sup> From a comparison of the single-exponent fits with two-exponent fits, we deduce that more than 85% of the temporally integrated CL emission can be described by an initial single-exponential fit.

The CL intensity vs time transients of the SQW peak emission acquired for sample S4 at low- and high-excitation densities are shown in Fig. 8(b) for  $T=280$  K. At low excitation a single-exponential behavior is observed, with 97% of the temporally integrated CL emission described by the initial single-exponential fit, and one decay time  $\tau$  is indicated. At high excitation, a double-exponential behavior is observed and two different decay times  $\tau_1$  and  $\tau_2$ , obtained by a linear fit of the two respective slopes in the decay curve, are indicated. As shown in Fig. 8(b), the initial decay time of  $\tau_1=23.4$  ns at high excitation, obtained by a linear fit of the initial slope in the decay curve, is significantly longer than the decay time of  $\tau_2=13.5$  ns and the decay time of  $\tau=10$  ns that was obtained by a linear fit at low excitation. Figure 8(b) shows the transition from an excitation range where most of carriers at high temperature recombine

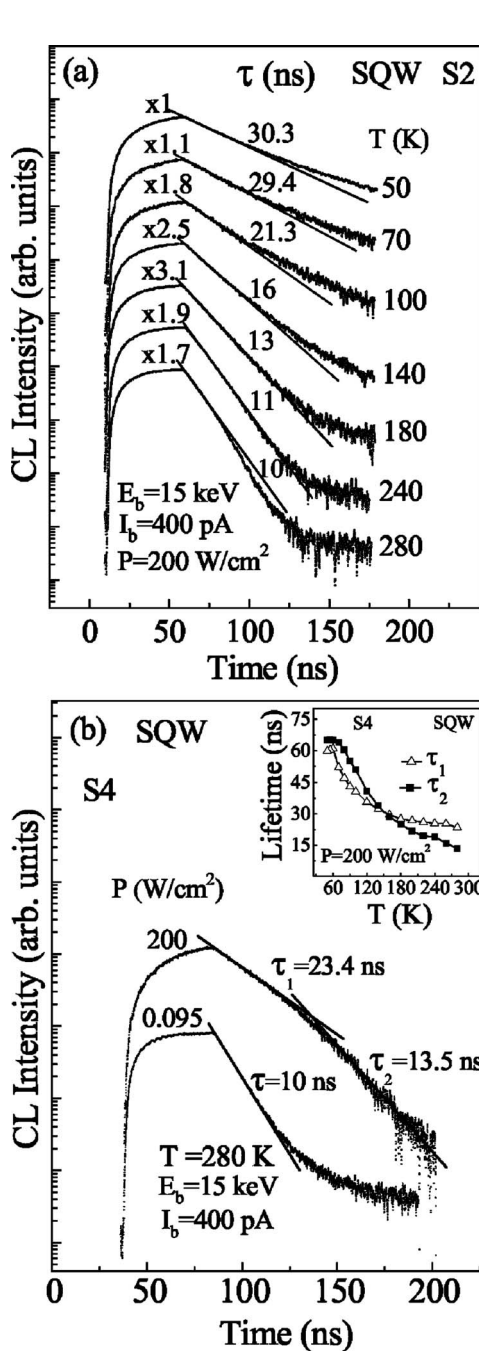


FIG. 8. (a) The CL transients including the onset and decay of the SQW peak luminescence for sample S2 acquired under high excitation,  $P=200 \text{ W/cm}^2$ , in  $50 \leq T \leq 280 \text{ K}$  temperature range. Initial decay times obtained by a linear fit are indicated for each temperature. All transients are scaled to have the same relative maximum intensity; scaling factors are indicated. (b) The CL transients including the onset and decay of the SQW peak luminescence for sample S4 acquired under low- and high-excitation at  $T=280 \text{ K}$ . Two different decay times  $\tau_1$  and  $\tau_2$ , obtained by a linear fit of the two respective slopes in the decay curve, are indicated at high excitation. At low excitation, a single-exponent decay with the time  $\tau$  is observed. The inset shows the decay times  $\tau_1$  and  $\tau_2$  of the SQW peak luminescence vs temperature for sample S4 at the high-excitation condition,  $P=200 \text{ W/cm}^2$ .

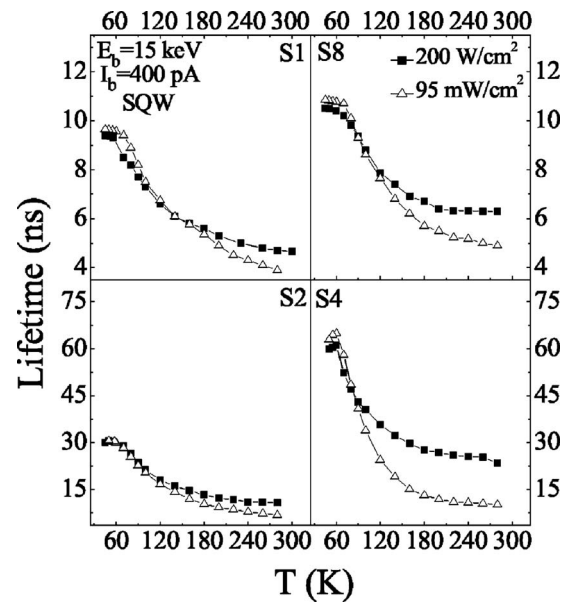


FIG. 9. The decay times  $\tau$  of the SQW peak luminescence vs temperature for samples S1–S8 under low- and high-excitation conditions of  $95 \text{ mW/cm}^2$  and  $200 \text{ W/cm}^2$ , respectively.

through nonradiative channels to a regime when a large fraction of the carriers recombine radiatively, owing to the saturation of nonradiative channels. The saturation of nonradiative channels naturally results in a greater contribution from radiative channels and leads to the longer lifetimes  $\tau_1$  and  $\tau_2$  relative to  $\tau$  (at low excitation). A similar behavior was observed for all samples S1–S8.

Furthermore, the decay times  $\tau_1$  and  $\tau_2$  of the SQW peak luminescence at high excitation,  $P=200 \text{ W/cm}^2$ , vs temperature are shown in the inset in Fig. 8(b) for sample S4. A slower decrease with temperature is observed for the initial decay time  $\tau_1$ , owing to a partial saturation of the nonradiative channels at higher excitation densities. A reversal of the lifetime behavior is observed for low and high temperatures, in which  $\tau_2$  is higher than  $\tau_1$  at low temperatures and  $\tau_2$  lower than  $\tau_1$  at high temperatures, as seen in the inset of Fig. 8(b). This supports the notion that at high temperatures, a greater fraction of carriers recombines through nonradiative channels, while at low temperatures ( $T < \sim 80 \text{ K}$ ) the radiative recombination processes become dominant.

In Fig. 9 we display initial decay lifetimes of the SQW peak emission as a function of temperature and excitation for samples S1–S8. Two clear trends are readily observed in Fig. 9. First, we note that decay lifetimes decrease more rapidly with an increasing temperature at lower excitation. Second, we observe that measured lifetimes saturate at temperatures below  $\sim 80 \text{ K}$ , owing to the decrease in nonradiative rates. At RT, much higher lifetimes are observed in all samples for the case of high-excitation density,  $P=200 \text{ W/cm}^2$ . Similar effects were observed in various isolated InGaN QW samples at high temperatures and attributed to the saturation of nonradiative recombination under high-excitation conditions.<sup>25,36,37</sup> At RT, when the excitation density is low, most of the excited carriers recombine through nonradiative channels. As the excitation density increases, a larger frac-

tion of the carriers will recombine radiatively due to the saturation of the nonradiative channels, and therefore the effective lifetime will increase.<sup>25,36–39</sup> At temperatures below  $\sim 80$  K an opposite trend is observed with equal or even higher decay lifetimes for a lower excitation density,  $P = 95$  mW/cm<sup>2</sup>. The decrease in measured decay lifetimes with an increase in excitation density can be attributed to an enhanced recombination rate due to the increased electron-hole wave function overlap, owing to excess carrier screening of internal fields under high excitation.

The behavior observed for the decay lifetime of the SQW peak emission at temperatures below  $\sim 80$  K, as shown in Fig. 9, strongly suggests that the radiative recombination process dominates at low temperatures. The differences in decay lifetimes of the SQW peak emission observed for different samples at low temperatures are most likely related to the differences in the magnitude of the electrical field, as caused by differences in the In composition or strain relaxation.<sup>40</sup>

The radiative lifetime at a given temperature can be estimated from a combined measurement of decay lifetime and integrated intensity using a standard expression for the radiative efficiency  $\eta$ :<sup>41–44</sup>

$$\eta(T) = \frac{\tau(T)}{\tau_R(T)} = \frac{I(T)}{I_0}, \quad (2)$$

where  $I_0$  is a normalization factor, which depends on the number of excited carriers and is equal to the value of the saturated CL intensity at low temperatures. The reciprocal of the spatially integrated CL intensity  $I^{-1}$  of the CR and SQW peak emission multiplied by decay lifetime  $\tau$  vs temperature was measured for samples S1–S8 at high constant excitation density, as shown in Fig. 10. If temperature-induced variations in both the CL intensity and decay lifetime are determined by nonradiative processes only, then the expression  $\tau I^{-1}$  is proportional to the radiative lifetime, as given by Eq. (2). For a better presentation of these data, we normalized the expression  $\tau I^{-1}$  to its maximum value, as shown in Fig. 10. Normalized radiative lifetimes of the CR peak emission increase linearly with the temperature up to about 180 K, as seen in Fig. 10. Similar results are obtained for the normalized radiative lifetimes of the SQW peak emission for samples S2, S4, and S8 at temperatures below 180 K. This behavior is an unambiguous signature of the two-dimensional excitonic system, consistent with radiative recombination of free excitons at low temperatures.<sup>44–47</sup> This is to be compared with the temperature-independent behavior of the normalized radiative lifetime of the SQW peak emission obtained for sample S1 at low temperatures, as seen in Fig. 10. The radiative lifetimes are expected to be temperature independent for fully localized excitons.<sup>44</sup> The behavior observed for sample S1 at low temperatures can be attributed to a strong carrier localization, confirmed by the previous results of Fig. 5. The decrease in the value of the normalized expression  $\tau I^{-1}$  for the SQW peak at temperatures above 180 K, as seen in Fig. 10 for samples S2–S8, is attributed to the thermally activated process of carrier transfer from the CR into the SQW, which is efficient at high temperatures. The onset of the thermally activated process of carrier trans-

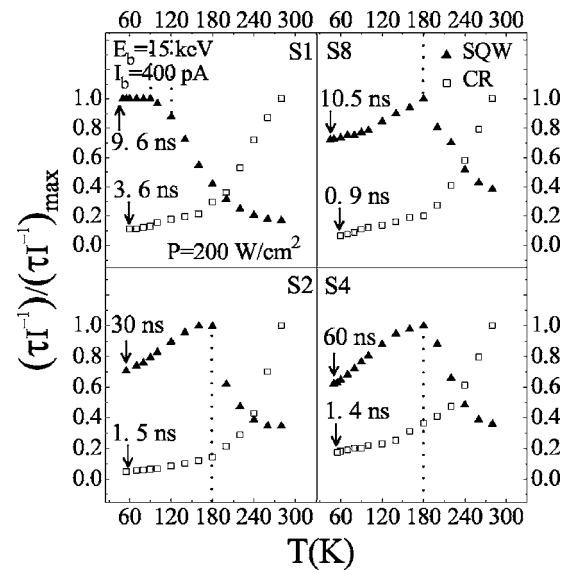


FIG. 10. Values of  $\tau I^{-1}$  (product of the decay lifetime and reciprocal CL intensity) for the CR (open squares) and SQW peak emission (triangles) normalized to its maximum value  $(\tau I^{-1})_{\max}$  vs temperature for samples S1–S8 at high-excitation density,  $P = 200$  W/cm<sup>2</sup>. For the CR peak emission and the SQW peak emission at temperatures below 180 K, this expression represents the normalized radiative lifetime. The onset of the temperature-dependent carrier transfer from the CR into the SQW is indicated by vertical dotted lines. The approximate radiative lifetime  $\tau_R$  for each sample at  $T = 50$  K is indicated with arrows.  $\tau_R$  can be obtained for higher temperatures by simple linear scaling for each sample.

fer into the SQW is indicated by vertical dotted lines, as shown. By comparing Figs. 4 and 10, a strong correlation is observed between the onset of the thermally activated process of carrier transfer into the SQW and the onset of rapid increase in the CL intensity of the SQW emission with increasing temperature. In both cases, sample S1 shows the lowest onset temperature, consistent with the lowest activation energy of  $\sim 60$  meV as determined for the CR peak emission in the 200 to 300 K temperature range (inset of Fig. 3). This behavior will be explained in Sec. V as a result of a reduced actual In composition and effective barrier height for thermal re-emission from the CR QW for sample S1.

As shown experimentally in Figs. 9 and 10, the decay lifetimes of the SQW peak emission determined at temperatures below 70 K are close to (i) the radiative lifetimes of free excitons for the three samples S2, S4, and S8 and (ii) the radiative lifetimes of localized excitons for the single sample S1. By approximating the experimentally measured decay lifetimes of the SQW peak emission at  $T = 50$  K with the radiative lifetimes of free and/or localized excitons, the temperature dependence of radiative lifetimes is also simultaneously observed in Fig. 10. The approximate radiative lifetime for each sample at  $T = 50$  K is indicated with arrows in the figure.

At low and intermediate temperatures, when emission from the CR dominates in the spectra, as seen from Fig. 2(b), the relationship between the steady-state carrier density  $n_{\text{CR}}$  in the CR and the excitation density  $P$  can be approximated by

$$n_{\text{CR}} \approx \frac{P\tau_{\text{QW}}}{3E_g}, \quad (3)$$

where  $E_g$  is the bandgap of GaN and  $\tau_{\text{QW}}$  is the carrier lifetime in QWs of the CR. We estimated the steady-state carrier sheet densities  $n_{\text{CR}}$  in the confinement region at  $T=58$  K and  $P=200$  W/cm<sup>2</sup> as  $4.4 \times 10^{11}$ ,  $1.8 \times 10^{11}$ ,  $1.7 \times 10^{11}$ , and  $1.1 \times 10^{11}$  cm<sup>-2</sup> for samples S1–S8, respectively.

### C. Total luminescence efficiency

We observe that the integrated CL intensities of the GaN, CR, and SQW emission for all samples, both at low- and high-excitation density, start to saturate at temperatures below 80 K, as partially seen in Figs. 3 and 4. From the saturation behavior of the CL intensities, we assume that the total luminescence efficiency  $\eta_T$  of emission for these samples is  $\sim 1$  at  $T=50$  K. We measured nearly equal values of the total integrated CL intensity  $I_T$  [which is equal to the sum of integrated CL intensities of the GaN ( $I_{\text{GaN}}$ ), CR ( $I_{\text{CR}}$ ), and SQW ( $I_{\text{SQW}}$ ) emission] obtained for samples S2, S4, and S8 at  $T=50$  K. We estimate by an intensity comparison that  $\eta_T$  for sample S1 at  $T=50$  K is  $\sim 0.6$  at high-excitation density and is  $\sim 0.5$  at low-excitation density, owing to the absence of a saturation effect at  $T=50$  K for this sample. The total luminescence efficiency at any arbitrary temperature  $T$  for  $T > 50$  K is obtained from the expression  $\eta_T = I_T(T)/I_T(50 \text{ K})$ . The total luminescence efficiencies at both low- and high-excitation densities and different temperatures in  $50 \leq T \leq 300$  K range are shown in Fig. 11 for all samples. In addition, the emission fraction  $F_i$  indicating the relative weights of each of the GaN, CR, and SQW components is also plotted in Fig. 11.  $F_i$  is defined as the ratio of the integrated CL intensity for each component  $i$  (GaN, CR, and SQW) to the total integrated CL intensity for a given temperature (i.e.,  $F_{\text{GaN,CR,SQW}} = I(T)_{\text{GaN,CR,SQW}}/I_T(T)$  and  $\sum F_i = 1$ ). Emission at low temperatures is dominated by the CR emission with  $F_{\text{CR}} \approx 0.7$ , while at high temperatures the largest emission weight is from the SQW. The rapid increase in  $F_{\text{SQW}}$  at higher temperatures indicates a strong carrier transfer into the SQW, consistent with the previous results. A comparison of Figs. 11(a) and 11(b) shows that  $F_{\text{SQW}}$  grows faster with temperature at high-excitation densities, owing to the enhanced filling of QWs in the CR and saturation of nonradiative channels in the SQW. At RT, the highest total luminescence efficiency of  $\sim 60\%$  is observed at high-excitation density for samples S1 and S8. Further, as  $P$  increases from  $95$  mW/cm<sup>2</sup> to  $200$  W/cm<sup>2</sup> at RT, the total luminescence efficiency  $\eta_T$  of samples S1 and S8 increases from  $\sim 30\%$  to  $\sim 60\%$ .

### IV. THEORETICAL MODEL

In order to model our CL data, determine values of electric field in the QWs of the CR and SQW, and to model nonlinear effects associated with carrier capture from the CR into the SQW, we solved self-consistently the Schrödinger and Poisson equations, within a single-band effective mass approximation. By doing so, we calculate the electron and

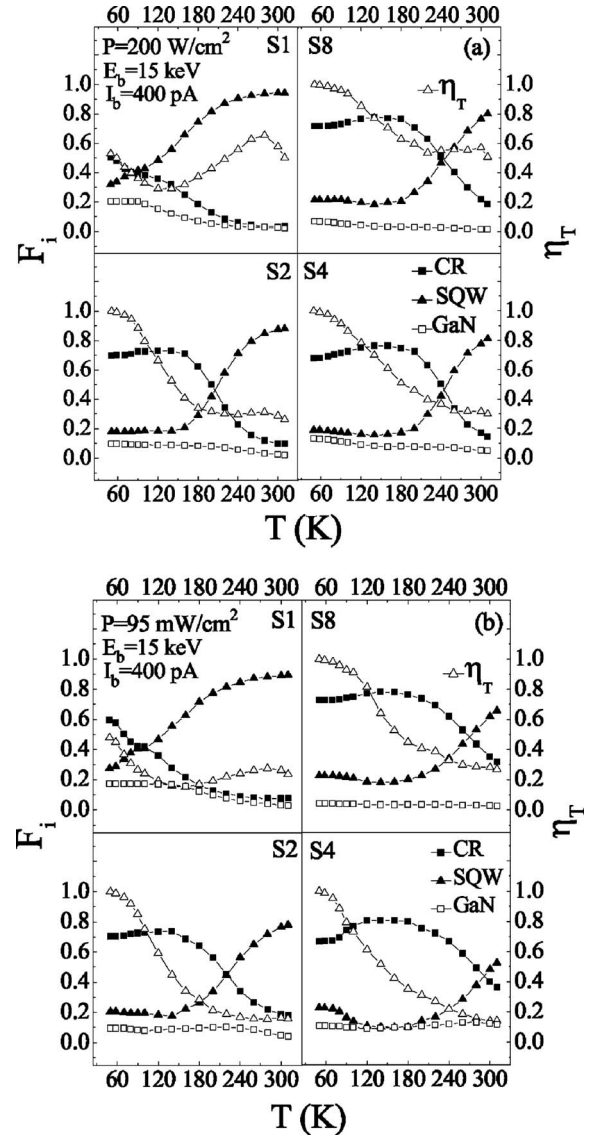


FIG. 11. The total luminescence efficiency  $\eta_T$  (open triangles) and the emission fraction  $F_i$  from the GaN (open squares), CR (squares), and SQW (triangles) at different temperatures in the  $50 \leq T \leq 300$  K range for samples S1–S8 at (a) high- and (b) low-excitation density. The total luminescence efficiency  $\eta_T$  of samples S2, S4, and S8 is close to 100% at  $T=50$  K, while a lower initial  $\eta_T$  of  $\sim 60\%$  at  $T=50$  K and high-excitation density was estimated for sample S1. At RT, the highest total luminescence efficiency of  $\sim 60\%$  is observed at high-excitation density for samples S1 and S8. As the excitation density  $P$  increases from  $95$  mW/cm<sup>2</sup> to  $200$  W/cm<sup>2</sup>,  $\eta_T$  for samples S1 and S8 at RT changes from  $\sim 30\%$  to  $\sim 60\%$ .

hole wave functions and energy levels while taking into account the modifications of the potential profile caused by the accumulation of carriers in QWs of the CR and SQW. Band-edge and effective mass parameters were first obtained from a strain- and In composition-dependent  $k \cdot p$  calculation for wurtzite  $\text{In}_x\text{Ga}_{1-x}\text{N}$ , using a  $6 \times 6$   $k \cdot p$  Hamiltonian in the  $\{0001\}$  representation.<sup>48</sup> The relevant parameters in the  $k \cdot p$  method for a wurtzite crystal include the  $A_i$ 's, which are similar to the Luttinger parameters in a zinc-blende crystal;

the  $D_i$ 's, which are the deformation potentials for the  $\text{In}_x\text{Ga}_{1-x}\text{N}$  layers;  $c_{ij}$ 's the elastic constants, and  $\varepsilon_{ij}$ , the strain tensor elements.<sup>48</sup> The  $\mathbf{k}\cdot\mathbf{p}$  parameters for  $\text{In}_x\text{Ga}_{1-x}\text{N}$  were obtained by linearizing between those for InN and GaN for a given composition  $x$ . The strain tensor components  $\varepsilon_{ij}$ , along with the piezoelectric tensor elements  $d_{ijk}$  and spontaneous polarization parameter  $P_{\text{sp}}$ , are also used to calculate the polarization of the well (barrier) material along the (0001) axis.<sup>49</sup> All numerical parameters that were employed in our  $\mathbf{k}\cdot\mathbf{p}$  and polarization calculations are available in Ref. 50. After a determination of the valence band energy dispersions for a given In composition, the heavy- and light-hole effective masses for dispersion along  $\langle 0001 \rangle$  and the average in-plane effective masses were determined. The electron effective masses for dispersion in the QW  $x$ - $y$  plane and along the QW  $z$  direction are obtained by a linearization between values for InN and GaN.<sup>50</sup> The conduction to valence band offset in wurtzite  $\text{In}_x\text{Ga}_{1-x}\text{N}$  is assumed to be independent of  $x$ , and is taken as  $\Delta E_c/\Delta E_v=70/30$ , as has been proposed recently by different researchers.<sup>24,50-52</sup> We take the unstrained  $\text{In}_x\text{Ga}_{1-x}\text{N}$  bandgap at an arbitrary temperature as previously determined.<sup>53,54</sup> The strain-induced increase in the bandgap is given by solutions from the  $\mathbf{k}\cdot\mathbf{p}$  calculations which included the deformation potentials for a particular strain tensor.<sup>50</sup>

To construct an initial potential profile we used the following assumptions: (i) the potential energies on the far right and far left of the MQW structure are the same<sup>55,56</sup> and (ii) the potential drop over the confinement region is independent of that over the SQW and capping layer and is equal to zero. The second assumption (ii) allows for a decoupling of the CR and SQW regions and enables the determination of the internal electric field in the QWs for these regions independently. From (i) and (ii) with an additional assumption that the electric displacement is conserved along the growth axis,<sup>55,57</sup> we obtain

$$E_W^{\text{CR}} = -\frac{E_B L_B}{L_W^{\text{CR}}} = \frac{L_B(P_B - P_W^{\text{CR}})}{(\varepsilon_W^{\text{CR}} L_B + \varepsilon_B L_W^{\text{CR}})},$$

$$E_W^{\text{SQW}} = -\frac{E_C L_C}{L_W^{\text{SQW}}} = \frac{L_C(P_B - P_W^{\text{SQW}})}{(\varepsilon_W^{\text{SQW}} L_C + \varepsilon_B L_W^{\text{SQW}})}, \quad (4)$$

where  $L_w$ ,  $L_B$ , and  $L_C$  are the well, barrier, and capping layer widths, respectively,  $\varepsilon_w$  ( $\varepsilon_B$ ) is the well (barrier) static dielectric constant,  $E_w$  ( $E_B/E_C$ ) is the electric field in the well (barrier/capping layer), and  $P_w$  ( $P_B$ ) is the polarization of the well (barrier) material, which includes both the piezoelectric and spontaneous polarizations. Superscripts denote the SQW and CR regions, respectively. Using Eq. (4), we estimate values of the electric field in the QWs of the CR with 5% In composition as 0.15 and 0.54 MV/cm for sample S1 with a 25 nm thick QW in the confinement region and the other three samples, respectively. For the SQW with a 12% In composition, the estimated value of the electric field is  $\sim 1.57$  MV/cm.

The energy levels and single-particle electron and hole wave functions,  $\psi_{e,h}(z)$  were determined by partitioning the structures into thin layers and using a finite-element tech-

nique, modified for the case of variable effective masses, to find solutions to the Schrödinger equation for a particle subject to an electric field.<sup>17,19,58,59</sup> For a given excess carrier concentration  $n$ , using the two-dimensional density of states which is proportional to the appropriate in-plane effective masses, we calculate the population of each quantized state and the quasi-Fermi levels for electrons and holes. The electron, heavy- and light-hole carrier densities in these quantized states can be determined by integrating the product of the two-dimensional (2D) density of states and the Fermi-Dirac function. The quasi-Fermi levels  $\phi_{e,h}$  are determined in the usual manner by conserving total electron and hole charges for a given excitation.<sup>59</sup> All bound hole and electron states were included in the calculations. The spectrum of energy states associated with the single-electron and hole wave functions,  $E_i^e$  and  $E_j^{hh}$ , as computed numerically, can be separated according to their localization in QWs of the CR and SQW. Using these eigenvalues, quasi-Fermi energy levels  $\phi_e$  and  $\phi_h$  for electrons and holes, each in the CR and SQW, were separately determined for a given steady-state carrier density. Given the population of each quantized level, we solved the nonlinear Poisson-Schrödinger equation for our four sample structures, including the effects of strain, deformation potentials, and piezoelectric field.<sup>60</sup> The total three-dimensional charge densities of electrons and heavy holes,  $\rho_e$  and  $\rho_{hh}$ , at any arbitrary position along the MQW growth direction  $z$  is obtained by summing the charge densities calculated for the CR and SQW.

The exciton binding energies  $E_B$  in QWs of the CR and SQW were determined by substitution of respective single-electron and hole wave functions, computed numerically using a finite-element technique, into a radial eigenvalue equation that involves the electron-hole relative motion in an effective in-plane Coulomb potential.<sup>50,61</sup> The estimated exciton binding energies in samples S1-S8 lie in the 2–7 meV range for the CR and in 25–31 meV range for the SQW. It was previously established that the exciton binding energy approaches zero for temperatures  $T \gg E_B/k_B$  and for carrier densities on the order of  $\sim 10^{11} \text{ cm}^{-2}$ .<sup>20</sup> Such densities are easily accessible in QWs of the CR for the high-excitation densities used in this study.

Using results from our calculations, the luminescence lineshape  $I(\hbar\omega)$  can be determined by the following expression:<sup>62</sup>

$$I(\hbar\omega) = \sum_{i,j} I_{ij}^2 \int_{E_i^e}^{\hbar\omega - E_g - E_j^{hh} + E_B \delta_{i1} \delta_{1j}} dE H(\hbar\omega - E_g - E_i^e - E_j^{hh} + E_B \delta_{i1} \delta_{1j}) g_{ij} f(E - \phi_e) f(\hbar\omega - E_g - E - \phi_h),$$

$$g_j = \frac{m_r^*}{\pi \hbar^2}, \quad (5)$$

where  $I_{ij}$  is the overlap integral for electron and hole envelope wave functions,  $f(E)$  is the Fermi-Dirac function,  $g_j$  is the 2D joint density of states, which contains the reduced mass term  $m_r^*$ , where  $1/m_r^* = 1/m_z^e + 1/m_z^{hh}$  and  $H(E)$ , the Heaviside function, is 0 for  $E < 0$  and is 1 for  $E \geq 0$ . Using the calculated values for the quasi-Fermi energies, we calcu-

lated  $I(\hbar\omega)$  for both the CR and SQW as a function of temperature and excitation. In addition, to include the effects of instrumental and inhomogeneous broadening, we have convolved  $I(\hbar\omega)$  with a Gaussian of width equal to the width of the narrowest optical transition, which was measured for lowest accessible temperatures and beam currents.<sup>62</sup> In our simple model, we allow for both (i) excitonic transition, by including the term  $E_B\delta_{i1}\delta_{1j}$ , where  $\delta_{i1}\delta_{1j}$  is 1 for  $i=j=1$  and 0 for all other cases, and (ii) band-to-band transitions between the higher-energy states. We do not include excitonic properties in the calculation of  $I(\hbar\omega)$  for the CR peak, owing to the high attainable carrier densities and low exciton binding energies calculated for the QWs of the CR, and so we set  $E_B=0$  in Eq. (5).

## V. APPLICATION OF THEORY TO EXPERIMENTAL RESULTS

### A. Measurement of the electric field and In composition for the SQW

Two different approaches were used to determine values of the electric field and In composition in the QWs of the CR and SQW. As shown experimentally, see Figs. 9 and 10, the decay lifetimes of the SQW peak emission determined at temperatures below 70 K are close to the radiative lifetimes of free and localized excitons for the three samples S2, S4, and S8 and the single sample S1, respectively. By using this experimental fact, values of the electric field ( $E_{\text{exp}}^{\text{SQW}}$ ), and In composition in the SQW can be estimated by fitting both the SQW peak energy position and decay lifetimes, that are approximated by radiative lifetimes of free or localized excitons, at low temperatures. In order to accomplish this, we calculated luminescence lineshapes and radiative lifetimes of free and localized excitons at  $T=50$  K for various values of the electric field and In composition, that were varied independently. Radiative lifetimes  $\tau_R$  of free excitons can be determined by solutions of the following equations:<sup>46,47,63</sup>

$$\frac{\partial\tau_R}{\partial T} = \frac{2M_X k_B}{\hbar^2 k_0^2} \tau_0, \quad (6)$$

$$\tau_0 = \frac{1}{2} \left[ \frac{k_0 n \omega_{\text{LT}} a_B^3 I_{eh}^2}{a_{\perp}^2} \right]^{-1},$$

where  $M_X$  is the 2D exciton effective mass,  $k_0=2\pi/\lambda_{\text{peak}}$  is the wave vector of the photon at the excitonic resonance,  $\tau_0$  is the intrinsic radiative lifetime of the 2D system,  $n$  is the background refractive index,  $\omega_{\text{LT}}$  is the longitudinal-transverse splitting of the exciton state in the bulk that we assume equal to 0.6 meV,<sup>47</sup>  $a_B$  is the exciton Bohr radius in bulk, and  $I_{eh}$  is the overlap integral of electron and hole envelope wave functions normal to the QW plane. We take  $\lambda_{\text{peak}}$  equal to the experimentally measured wavelength of the SQW peak. The in-plane effective Bohr radius  $a_{\perp}$  was determined by substitution of the trial in-plane wave function  $\Phi_{e-h} = \sqrt{2/\pi} a_{\perp}^{-2} \exp(-r/a_{\perp})$  into the exciton eigenvalue equation with already known exciton binding energy  $E_B$ .<sup>50,61</sup> Radiative lifetimes  $\tau_R$  of localized excitons can be determined

likewise by substitution of calculated overlap integral of electron and hole envelope functions  $I_{eh}$  into<sup>47,63</sup>

$$\tau_R = 3 \left[ \omega_{\text{LT}} (k_0 n a_B)^3 I_{eh}^2 \frac{16R_e^2 R_h^2}{(R_e + R_h)^4} \right]^{-1}, \quad (7)$$

where  $R_e$  and  $R_h$  are electron and hole localization radii in the plane of the QW. Equation (7) simplifies if we take  $R_e = R_h$ , the simplest and most natural assumption.<sup>47</sup>

### B. A determination of the electric fields and In compositions for the CR

A different approach was employed to determine fields ( $E_{\text{exp}}^{\text{CR}}$ ) and In compositions in QWs of the CR. This is related to the fact that even at low temperatures, the approximation of the decay lifetimes of the CR peak emission by the radiative lifetimes is not valid, owing to the carrier transfer from the CR into the SQW. We have taken into account the large excess carrier densities in QWs of the CR at low temperatures that can be sufficient to partially screen its internal fields. Such screening effects and the subsequent blue shifting of the CR emission with increase in the excitation densities were observed for all samples. The most pronounced effect is observed for sample S1 with a single 25 nm thick QW in the CR. Figure 12(a) shows spatially integrated CL spectra acquired with a focused and strongly defocused electron beam for sample S1 at various beam currents at  $T=58$  K. Excitation densities  $P$  calculated using Eq. (1) are indicated. The various peaks, previously identified, are indicated by vertical dashed lines. Since the lineshape and energy position of the SQW peak remains nearly constant over five orders of magnitude of excitation (at  $T=58$  K), we can assume that carrier filling and screening in the SQW are negligible under the present excitation conditions and temperature. A vertical dashed line in Fig. 12(a) indicates a blue shift of  $\sim 85$  meV in the CR peak position as  $P$  increases from 7 mW/cm<sup>2</sup> to 200 W/cm<sup>2</sup>. The full widths at half-maximum (FWHM) of these spectra decrease from 290 to 136 meV over this range, indicating that a large blue shift in the CR peak position is related to the carrier screening of the internal electric fields.

In order to simulate these effects, we calculated the luminescence lineshapes of the CR emission at different excess carrier densities for various values of the electric field and In composition. Both the field and the composition were varied independently. Correct values of the electric field and In composition were determined by fitting the CR peak position at low and high carrier densities so that the observed experimental blue shift, resulting from carrier screening of internal electric fields, is reproduced. Figure 12(b) shows calculated and normalized luminescence lineshapes of the CR emission for various excess carrier densities in the  $0.14\text{--}4.4 \times 10^{11}$  cm<sup>-2</sup> range at  $T=58$  K. A blue shift in the position of maximum peak intensity and narrowing of the FWHM of  $I(\hbar\omega)$  with increase in the excess carrier densities are readily observed.

The inset in Fig. 12(b) shows the excess carrier densities in the CR and SQW vs excitation density  $P$  for sample S1 at  $T=58$  K. Similar results were obtained for the other samples.

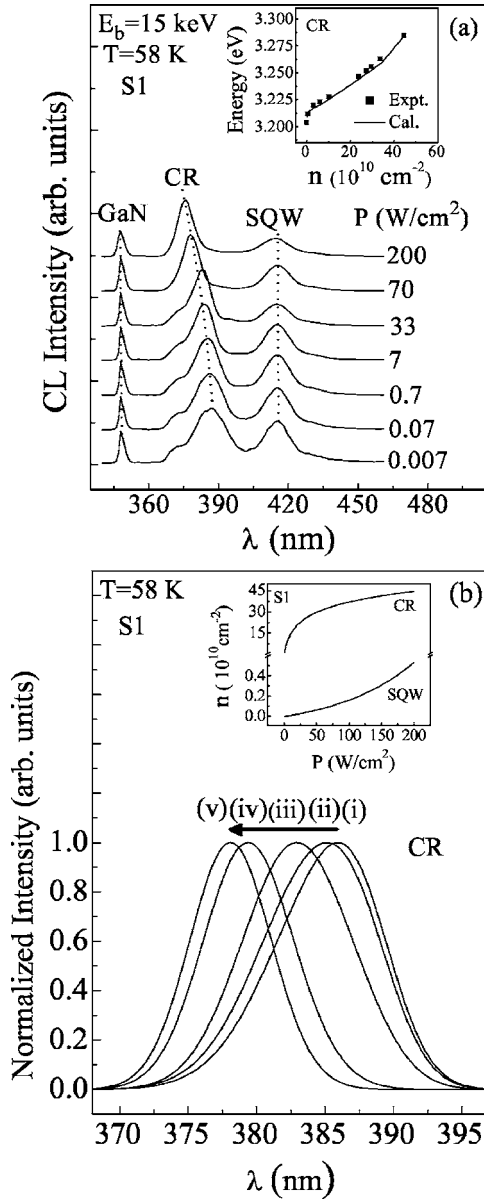


FIG. 12. Spatially integrated CL spectra of sample S1 acquired for various excitation densities  $P$  in (a) and calculated luminescence lineshapes of the CR emission in (b) for the structure of sample S1 with carrier densities  $n_{CR}$  of (i) 0.14, (ii) 1, (iii) 2, (iv) 3, and (v)  $4.4 \times 10^{11} \text{ cm}^{-2}$ . Both the experimental and calculated lineshapes show the blue shift with increasing excess carrier concentration, at  $T=58 \text{ K}$ . A vertical dashed line in (a) indicates a blue shift of  $\sim 85 \text{ meV}$  in the CR peak position as  $P$  increases from  $7 \text{ mW/cm}^2$  to  $200 \text{ W/cm}^2$ . The inset in (a) shows the experimental (squares) and calculated (solid line) energies of the CR peak intensity position vs excess carrier density for sample S1 at  $T=58 \text{ K}$ . The inset in (b) shows the excess carrier density  $n$  in both the CR and SQW vs excitation for sample S1 at  $T=58 \text{ K}$ .

Carrier densities in the CR,  $n_{CR}$ , were first approximated with Eq. (3) by using values of the excitation density  $P$  and experimentally measured carrier lifetimes of the CR,  $\tau_{QW}$ . Carrier densities in the SQW were then determined for the calculated values of  $n_{CR}$  from our model, as described in Sec. V C. The observed nonlinear variation in the excess carrier

TABLE I. Values of the electric field and In composition  $x$  in QWs of the CR and SQW, as determined by different approaches for the MQW samples of this study.

Sample N	S1	S2	S4	S8
InN mole fraction in QWs of the CR	0.034	0.060	0.056	0.058
Measured field value in QWs of the CR $E_{exp}^{CR}$ (MV/cm)	0.09	0.63	0.60	0.42
Calculated field value in QWs of the CR using Eq. (4) $E_{theory}^{CR}$ (MV/cm)	0.10	0.65	0.60	0.62
InN mole fraction in the SQW	0.104	0.115	0.126	0.120
Measured field value in the SQW $E_{exp}^{SQW}$ (MV/cm)	1.27	1.47	1.71	1.06
Calculated field value in the SQW using Eq. (4) $E_{theory}^{SQW}$ (MV/cm)	1.33	1.49	1.66	1.55
Calculated exciton binding energy in the SQW $E_B$ (meV)	26.5	26.3	25.1	29.7
Calculated in-plane Bohr radius in the SQW $a_{\perp}$ (nm)	2.84	2.88	3.15	2.37

density in the CR with excitation density  $P$ , as seen in the inset in Fig. 12(b), is caused by a decrease in measured decay lifetime of the CR emission with an increase in excitation density, owing to excess carrier screening of internal electric fields under high excitation.<sup>17–19</sup> At the same time, the increase in the excess carrier density in the SQW with increasing excitation  $P$  results from band filling in QWs of the CR at high excitation followed by a subsequent transfer of carriers to the SQW, as shown in Sec. III A. The inset of Fig. 12(a) further shows the experimental and calculated energies of the CR peak vs excess carrier density.

Values of the electric field and In composition determined by both approaches for the four samples, are summarized in Table I. In addition, values of the electric field calculated using Eq. (4), the in-plane Bohr radius, and exciton binding energies calculated for the SQW are included in this table. As seen from Table I, within the margins of error ( $\sim 5\text{--}10\%$ ), the derived electric field values for samples S1, S2, and S4 are equal to the electric field values calculated using Eq. (4). However, for sample S8,  $\sim 30\%$  lower electric field values are obtained, owing likely to the strain relaxation that is often observed in thick InGaN MQW structures.<sup>40</sup> The CL imaging (not shown) of the CR emission ( $\lambda=377 \text{ nm}$ ) for sample S8 exhibited the presence of dark line defects indicative of misfit dislocations and a clear sign of strain relaxation. These defects were not detected in the CL imaging of samples S1–S4. The measured electric field value of the SQW for sample S8 is also the lowest among all four samples, as seen from Table I.

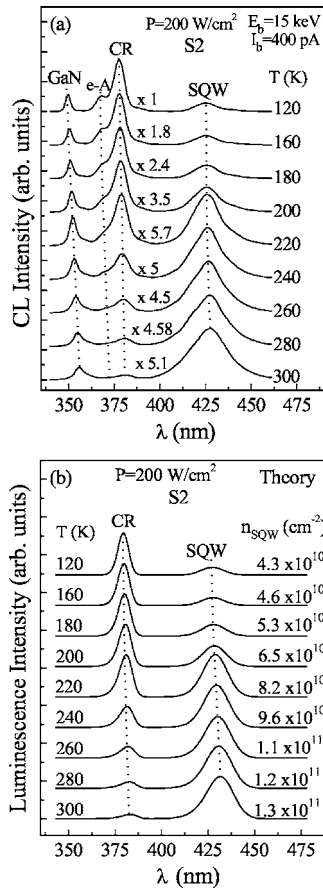


FIG. 13. Experimental spatially integrated CL spectra of sample S2 (a) and calculated luminescence lineshapes of the CR and SQW peaks for the same structure (b) at various temperatures for the high-constant excitation condition of  $P=200 \text{ W/cm}^2$ . The CR and the SQW emission peaks are indicated by vertical dashed lines. Carrier densities in the SQW determined by the model are indicated in (b) for various temperatures.

The lowest In composition in the QWs of the CR and SQW were calculated for sample S1, as seen in Table I. It is significant to note that for sample S1, the reduced electron and hole barrier heights for the QWs of the CR caused by this lower actual In composition (compared to the nominal composition of 5% attempted in the growth) are very much consistent with (i) the lowest activation energy for carrier thermal re-emission for the CR and (ii) the lowest onset temperature for a rapid increase of the SQW luminescence, as seen in the experimental results of Figs. 3 and 4.

### C. Modeling the temperature dependence of the SQW and CR luminescence

Figure 13(a) shows spatially integrated and constant excitation CL spectra of sample S2 acquired under a high-excitation condition,  $P=200 \text{ W/cm}^2$ , at various temperatures. All spectra are normalized to have nearly the same intensity; the scaling factors are indicated. The CR and the SQW emission peaks are indicated by vertical dashed lines. The peak labeled as e-A at 3.7 eV is identified as a free electron to acceptor transition in bulk GaN.<sup>50</sup>

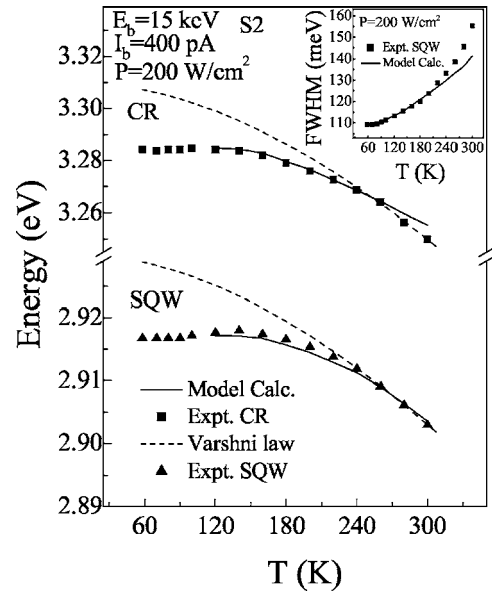


FIG. 14. Experimental and calculated energies of the CR (squares) and SQW (triangles) peak intensity positions vs the temperature for sample S2 with excitation condition  $P=200 \text{ W/cm}^2$ . The solid lines show the position of maximum peak intensity of  $I(\hbar\omega)$  for the CR and SQW. The dashed lines represent the fit according to the Varshni equation. The inset shows experimental (squares) and calculated (solid line) full widths at half-maximum (FWHM) of the SQW luminescence lineshape vs the temperature.

By utilizing the previously determined values of the electric field and In composition, the luminescence lineshapes of the CR and SQW peaks were calculated at different temperatures and excitations. Carrier densities in the confinement region were first approximated by Eq. (3) for a given initial temperature  $T_0$ , lower than the temperature corresponding to the onset of the SQW peak intensity increase (as seen in Fig. 4). Carrier densities in the SQW at that temperature can be determined by fitting the ratio of the experimental CR and SQW peak CL intensities,  $I_{\text{peak}}^{\text{CR}}(T_0)/I_{\text{peak}}^{\text{SQW}}(T_0)$ , to the values obtained from the simulated CL spectra, such as those shown in Fig. 13(b). Carrier densities in the CR and SQW at larger temperatures were then determined by comparison of simulated and experimental CL spectra. Calculated CL spectra of the CR and SQW peaks, from which carrier densities were determined in the fitting procedure, are shown in Fig. 13(b) for sample S2 at various temperatures in the  $120 \leq T \leq 300 \text{ K}$  range. Calculated carrier densities in the SQW are indicated for different temperatures.

The experimental and calculated energies of the CR and SQW peak intensity positions, as determined by a Gaussian fit from the experimental and the calculated spectra of sample S2 are plotted vs  $T$  in Fig. 14. The dashed lines represent the fitting according to the simple Varshni relation. The calculated CR and SQW peak energies show a good agreement with experiment for a wide range of temperatures, while the Varshni equation gives a reasonable fit only for temperatures higher than  $\sim 200 \text{ K}$ . Similar results (not shown) were also obtained for samples S4 and S8. A large deviation of the calculated SQW peak energies from those measured experimentally was obtained for sample S1, most

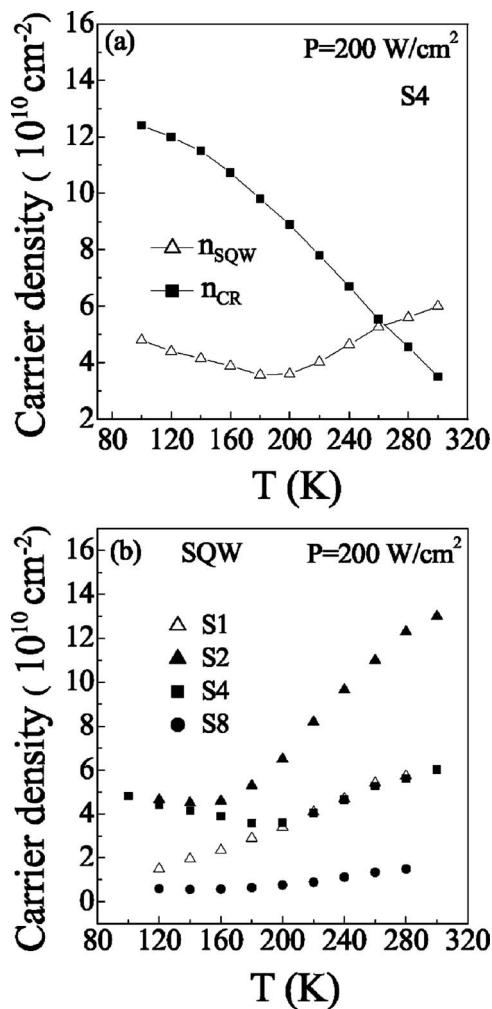


FIG. 15. The temperature dependence of the carrier density  $n(T)$  in the CR and SQW for sample S4 in (a) and for the SQW for samples S1–S8 in (b), as determined by the model calculations at various temperatures under high-excitation condition,  $P = 200 \text{ W/cm}^2$ .

likely due to the strong carrier localization observed in that sample. The inset of Fig. 14 shows the experimental and calculated FWHM of the SQW luminescence at various temperatures in the  $60 \leq T \leq 300 \text{ K}$  range. A reasonable agreement between theory and experiment is observed for temperatures below  $\sim 200 \text{ K}$ , while at higher temperatures the experimentally measured FWHM increases more rapidly with temperature. Figure 15(a) shows carrier densities in the CR and SQW, determined by model calculations for sample S4 vs temperature at high-excitation density,  $P = 200 \text{ W/cm}^2$ . In Fig. 15(a), the carrier density in the CR decreases with an increase in temperature which correlates well with the behavior of the experimental integrated CL intensity of the CR emission (as shown in Fig. 3), which decreases with increasing temperature. Such behavior is evidently due to the increasing role of nonradiative processes and an increased rate of carrier transfer and capture into the SQW at higher temperatures. Moreover, this is also well correlated with an increase in both the calculated carrier density and experimental integrated CL intensity of the SQW emis-

sion for increasing temperatures above 180 K. For comparison, the calculated carrier densities in the SQW for samples S1–S8 under the same high-excitation condition,  $P = 200 \text{ W/cm}^2$ , are shown in Fig. 15(b) for various temperatures in the  $120 \leq T \leq 300 \text{ K}$  range.

#### D. A determination of carrier capture and recombination rates in the SQW

In order to better understand the dynamical aspects of carrier capture into the SQW, we used the following rate equation model for the time evolution of the carrier density in the SQW:

$$\frac{dn}{dt} = R_C - \frac{n}{\tau_r} - \frac{n}{\tau_{nr}} = R_C - \frac{n}{\tau}, \quad (8)$$

where  $R_C$  is the carrier capture rate into the SQW and  $n$  is the minority carrier density in the SQW. Under steady-state conditions and assuming that  $R_C$  is constant for a given temperature and excitation, Eq. (8) becomes  $R_C(T) = n(T)/\tau(T)$ . The carrier capture rate into the SQW can be determined at any temperature for known values of  $n(T)$  and  $\tau(T)$ . The carrier capture rates for capture into the SQW, calculated from  $R_C = n/\tau$  at the high-excitation condition, are shown in a log  $R_C$  vs  $1/k_B T$  plot in Fig. 16(a) for all four samples. The solid lines indicate the results of linear fits in the temperature range of 180 to 300 K, from which corresponding activation energies are determined. Two clear trends are readily observed in Fig. 16(a). First, we note that carrier capture rates decrease with an increase in number of QWs in the confinement region. Second, a similar temperature behavior with small differences in the activation energies is observed for all samples at high temperatures, above 180 K, indicating that thermal escape of carriers from QWs of the CR is a dominant process responsible for carrier transfer and capture into the SQW at high temperatures. The differences in activation energies are related to differences in the In composition (and resulting barrier heights) in the QWs of the CR, as shown in Table I, with the lowest In composition and activation energy corresponding to sample S1. Dotted lines in Fig. 16(a) are shown to emphasize differences in the low-temperature behavior between sample S1 and samples S2, S4, and S8. A combination of experiment and theory shows that the rates for carrier capture into the SQW for samples S2, S4, and S8 are temperature independent for  $T < \sim 100 \text{ K}$ , as seen in Figs. 7 and 16(a). This behavior strongly suggests that carrier tunneling is the dominant process responsible for carrier transfer from the CR into the SQW at low temperatures. A markedly different behavior observed for sample S1 at low temperatures indicates that thermal escape of carriers from the QW of the CR is the dominant process responsible for carrier transfer and capture into the SQW for that sample in the  $60 \leq T \leq 300 \text{ K}$  temperature range.

Finally, the nonradiative (NR) recombination rates  $R_{\text{NR}}$  have been extracted for samples S2–S8 from a combination of the carrier capture rates and the temperature dependence of the SQW luminescence which is proportional to the radiative recombination rate  $R_R$ . The calculations for sample S1 are excluded here because we lack the data at sufficiently

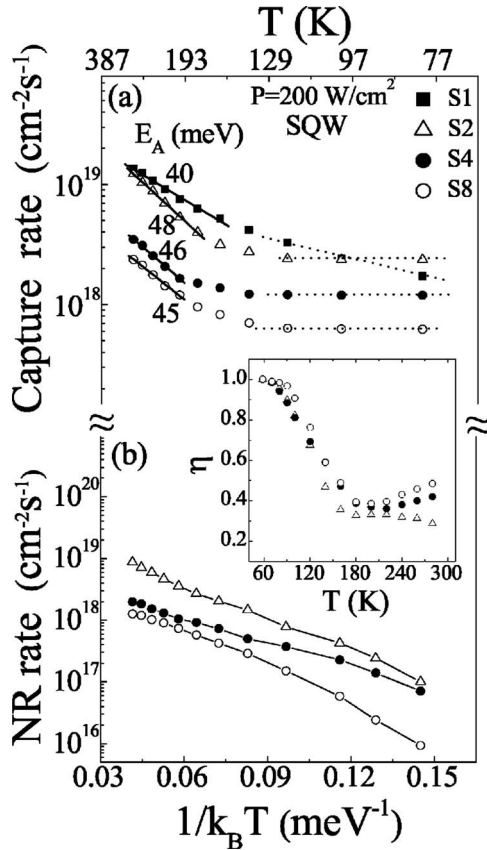


FIG. 16. Semi-log plots of the SQW carrier capture rates (a) and nonradiative (NR) recombination rates (b) vs  $1/k_B T$  under high-excitation condition,  $P=200 \text{ W/cm}^2$ . The solid lines in (a) indicate the results of linear fits in the temperature range of 180–300 K, from which corresponding activation energies are determined. The temperature-independent behavior of samples S2, S4, and S8 at low temperatures is indicated by horizontal dotted lines. The quantum efficiency of luminescence  $\eta$  for the SQW is shown for  $60 \leq T \leq 300$  K in the inset.

low temperatures in which  $\tau_R \approx \tau$  and  $R_{\text{NR}} \approx 0$ . Figure 16(b) shows that the NR recombination rate decreases with an increase in the number of QWs (i.e., in the sequence of samples S2–S8). Thus, the reduced capture rate is balanced by a reduced NR recombination for samples with more QWs in the CR. This compensating reduced NR rate leads to a quantum efficiency of luminescence  $\eta$  for the SQW (the inset of Fig. 16 which is obtained by  $\eta = R_R/R_C$ ) that increases in the sequence S2–S8, consistent with the SQW CL intensity results of Figs. 4 and 11. We hypothesize that a reduced number of QWs in the CR leads to a more rapid transfer of carriers across the CR to the SQW. However, there appears to be an increase in defect-related NR channels in the SQW associated with a reduced number of QWs in the CR that leads to the overall decrease in the quantum efficiency  $\eta$ .

## VI. SUMMARY AND CONCLUSIONS

We have examined in detail the optical properties of coupled  $\text{In}_x\text{Ga}_{1-x}\text{N}/\text{GaN}$  SQW structures grown by MOCVD with placements of varying numbers of QWs in the confine-

ment region as a function of temperature and excitation. In order to study the effect of different confinement layers on the carrier capture and subsequent luminescence efficiency of the SQW emission, we applied, in a complementary way, temperature- and excitation-dependent CL spectroscopy, and time-resolved CL measurements of onset and decay rates of important spectral features.

We solved self-consistently Schrödinger and Poisson equations within a single band effective mass approximation, to determine the energy states, wave functions and radiative lifetimes of free and localized excitons and to calculate luminescence lineshapes for QWs of the CR and for the SQW at different temperatures and excitations. Band-edge and effective mass parameters were first obtained from a strain- and In composition-dependent  $\mathbf{k}\cdot\mathbf{p}$  calculation for wurtzite  $\text{In}_x\text{Ga}_{1-x}\text{N}$ , using a  $6 \times 6$   $\mathbf{k}\cdot\mathbf{p}$  Hamiltonian. A quantitative analysis was employed to determine values of the electric field and In composition  $x$ , and to estimate carrier densities and carrier capture rates into the SQW as a function of temperature and excitation.

Both theory and experiment indicate that the high luminescence efficiency of the samples at RT is caused by a rapid capture of carriers into QWs of the CR followed by a transfer and subsequent capture of these carriers into the SQW. Thermal re-emission of carriers at high temperatures and carrier tunneling from the ground-state levels in QWs of the CR at low temperatures were identified as major processes through which the carrier transfer occurred from the CR into the SQW. At high temperatures, the fastest onset rate of the SQW emission was observed for the sample possessing a single thick QW in the confinement region, owing to a reduced In composition and reduced effective barrier height (as determined from the calculations) for the QW of the CR. By applying model calculations to the experimental results, we determined that carrier capture rates decrease with an increase in number of QWs in the confinement region. However, the quantum efficiency of luminescence and luminescence intensity of the SQW increase with the number of identical QWs in the CR (i.e., in the sequence 2, 4, and 8 QWs in the CR).

A number of interesting effects such as a saturation of nonradiative recombination channels, partial screening of internal electric fields and state filling of QWs in the confinement region, all of which affect the carrier capture and subsequent luminescence efficiency, were observed under high-excitation density. At RT, the highest total luminescence efficiency observed in the samples changes from  $\sim 30\%$  at low-excitation density to  $\sim 60\%$  at high-excitation density, owing to a state filling of QWs in the confinement region and saturation of nonradiative recombination channels in both the CR and the SQW. Our study demonstrates a unique and systematic procedure for treating carrier transfer, capture, and recombination in MQWs coupled to SQWs for the  $\text{InGaN}$  system. As applications of III-nitride optoelectronics continue to grow for the replacement of incandescent lighting and use of blue lasers in storage devices, procedures for optimizing the design of the optically active region could benefit from our approach or similar methods employed to evaluate an optimized carrier collection, transfer, capture, and luminescence efficiency in appropriate QW or MQW structures.

## ACKNOWLEDGMENTS

This work was supported by the Israel Science Founda-

tion (ISF Grant 8/02-1), the ARPA Optoelectronics Technology Center (OTC), the Office of Naval Research, and the Solid-State Lighting and Display Center.

- <sup>1</sup>S. Nakamura, T. Mukai, and M. Senoh, *Jpn. J. Appl. Phys., Part 2* **30**, L1998 (1991); *Appl. Phys. Lett.* **64**, 1687 (1994).
- <sup>2</sup>S. Nakamura, M. Senoh, N. Iwasa, and S. Nagahama, *Jpn. J. Appl. Phys., Part 2* **34**, L797 (1995).
- <sup>3</sup>S. Nakamura, M. Senoh, S. Nagahama, N. Iwasa, T. Yamada, T. Matsushita, H. Kiyoku, and Y. Sigimoto, *Appl. Phys. Lett.* **68**, 2105 (1996); *Jpn. J. Appl. Phys., Part 2* **35**, L74 (1996).
- <sup>4</sup>K. Osamura, S. Naka, and Y. Murakami, *Solid State Commun.* **11**, 617 (1972); *J. Appl. Phys.* **46**, 3432 (1975).
- <sup>5</sup>I. H. Ho and G. B. Stringfellow, *Appl. Phys. Lett.* **69**, 2701 (1996).
- <sup>6</sup>K. P. O' Donnell, R. W. Martin, and P. G. Middleton, *Phys. Rev. Lett.* **82**, 237 (1999).
- <sup>7</sup>P. J. Hansen, Y. E. Strausser, A. N. Erickson, E. J. Tarsa, P. Kozodoy, E. G. Brazel, J. P. Ibbetson, U. Mishra, V. Narayana-murti, S. P. DenBaars, and J. S. Speck, *Appl. Phys. Lett.* **72**, 2247 (1998), and references therein.
- <sup>8</sup>A. D. Bykhovski, V. V. Kaminski, M. S. Shur, Q. C. Chen, and M. A. Khan, *Appl. Phys. Lett.* **68**, 818 (1996).
- <sup>9</sup>F. Bernardini, V. Fiorentini, and D. Vanderbilt, *Phys. Rev. B* **56**, R10024 (1997); *Phys. Rev. Lett.* **79**, 3958 (1997).
- <sup>10</sup>A. Zoroddu, F. Bernardini, P. Ruggerone, and V. Fiorentini, *Phys. Rev. B* **64**, 045208 (2001).
- <sup>11</sup>S. Chichibu, T. Azuhata, T. Sota, and S. Nakamura, *Appl. Phys. Lett.* **69**, 4188 (1996).
- <sup>12</sup>J. S. Im, H. Kollmer, J. Off, A. Sohmer, F. Scholz, and A. Hangleiter, *Phys. Rev. B* **57**, R9435 (1998).
- <sup>13</sup>D. A. B. Miller, D. S. Chemla, T. C. Damen, A. C. Gossard, W. Wiegmann, T. H. Wood, and C. A. Burrus, *Phys. Rev. Lett.* **53**, 2173 (1984).
- <sup>14</sup>P. Lefebvre, A. Morel, M. Gallart, T. Taliercio, J. Allegre, B. Gil, H. Mathieu, B. Damilano, N. Grandjean, and J. Massies, *Appl. Phys. Lett.* **78**, 1252 (2001).
- <sup>15</sup>T. Deguchi, K. Sekiguchi, A. Nakamura, T. Sota, R. Matsuo, S. Chichibu, and S. Nakamura, *Jpn. J. Appl. Phys., Part 2* **38**, L914 (1999).
- <sup>16</sup>P. Riblet, H. Hirayama, A. Kinoshita, A. Hirata, T. Sugano, and Y. Aoyagi, *Appl. Phys. Lett.* **75**, 2241 (1999).
- <sup>17</sup>P. Lefebvre, S. Kalliakos, T. Bretagnon, P. Valvin, T. Taliercio, B. Gil, N. Grandjean, and J. Massies, *Phys. Rev. B* **69**, 035307 (2004).
- <sup>18</sup>T. Kuroda and A. Tackeuchi, *J. Appl. Phys.* **92**, 3071 (2002).
- <sup>19</sup>S. Kalliakos, P. Lefebvre, and T. Taliercio, *Phys. Rev. B* **67**, 205307 (2003).
- <sup>20</sup>P. Bigenwald, A. Kavokin, B. Gil, and P. Lefebvre, *Phys. Rev. B* **61**, 15621 (2000).
- <sup>21</sup>X. Zhang, D. H. Rich, J. T. Kobayashi, N. P. Kobayashi, and P. D. Dapkus, *Appl. Phys. Lett.* **73**, 1430 (1998).
- <sup>22</sup>S. Nakamura, M. Senoh, S. Nagahama, N. Iwasa, T. Yamada, T. Matsushita, Y. Sigimoto, and H. Kiyoku, *Appl. Phys. Lett.* **69**, 4056 (1996); **70**, 1417 (1997).
- <sup>23</sup>J. Rosner, E. C. Carr, M. J. Ludowise, G. Girolami, and H. I. Erikson, *Appl. Phys. Lett.* **70**, 420 (1997).
- <sup>24</sup>M. S. Minsky, S. B. Fleischer, A. C. Abare, J. E. Bowers, E. L. Hu, S. Keller, and S. P. Denbaars, *Appl. Phys. Lett.* **72**, 1066 (1998).
- <sup>25</sup>M. Dworzak, T. Stempel, A. Hoffmann, G. Franssen, S. Grzanka, T. Suski, R. Czernecki, M. Leszczynski, and I. Grzegory, *Mater. Res. Soc. Symp. Proc.* **892**, 0892-FF32-02.1 (2006).
- <sup>26</sup>S. Keller, S. B. Fleischer, S. F. Chichibu, J. E. Bowers, U. K. Mishra, and S. P. DenBaars, *Phys. Status Solidi B* **216**, 269 (1999).
- <sup>27</sup>H. T. Lin, D. H. Rich, A. Konkar, P. Chen, and A. Madhukar, *J. Appl. Phys.* **81**, 3186 (1997).
- <sup>28</sup>U. Jahn, S. Dhar, O. Brandt, H. T. Grahn, and K. H. Ploog, *J. Appl. Phys.* **93**, 1048 (2003).
- <sup>29</sup>S. Khatsevich, D. H. Rich, Eui.-Tae. Kim, and A. Madhukar, *J. Appl. Phys.* **97**, 123520 (2005).
- <sup>30</sup>D. Bimberg, H. Munzel, A. Steckenborn, and J. Christen, *Phys. Rev. B* **31**, 7788 (1985).
- <sup>31</sup>P. G. Eliseev, P. Perlin, J. Lee, and M. Osinski, *Appl. Phys. Lett.* **71**, 569 (1997).
- <sup>32</sup>Y.-H. Cho, G. H. Gainer, A. J. Fischer, J. J. Song, S. Keller, U. K. Mishra, and S. P. Denbaars, *Appl. Phys. Lett.* **73**, 1370 (1998).
- <sup>33</sup>M. Hao, J. Zhang, X. H. Zhang, and S. Chua, *Appl. Phys. Lett.* **81**, 5129 (2002).
- <sup>34</sup>Y. Kawakami, K. Omae, A. Kaneta, K. Okamoto, Y. Narukawa, T. Mukai, and S. Fujita, *J. Phys., J. Phys.: Condens. Matter* **13**, 6993 (2001).
- <sup>35</sup>Q. Li, S. J. Xu, M. H. Xie, and S. Y. Tong, *J. Phys.: Condens. Matter* **17**, 4853 (2005).
- <sup>36</sup>H. D. Sun, R. Macaluso, S. Calvez, G. J. Valentine, D. Burns, M. D. Dawson, K. Gundogdu, K. C. Hall, and T. F. Boggess, *J. Appl. Phys.* **96**, 1418 (2004).
- <sup>37</sup>C. Jordan, J. F. Donegan, J. Hegarty, B. J. Roycroft, S. Taniguchi, T. Hino, E. Kato, N. Noguchi, and A. Ishibashi, *Appl. Phys. Lett.* **74**, 3359 (1999).
- <sup>38</sup>K. Köhler, H.-J. Polland, L. Schultheis, and C. W. Tu, *Phys. Rev. B* **38**, 5496 (1988).
- <sup>39</sup>G. Bastard, E. E. Mendez, L. L. Chang, and L. Esaki, *Phys. Rev. B* **28**, 3241 (1983).
- <sup>40</sup>J. Bai, T. Wang, and S. Sakai, *J. Appl. Phys.* **90**, 1740 (2001).
- <sup>41</sup>R. C. Miller, D. A. Kleinman, W. A. Nordland, Jr., and A. C. Gossard, *Phys. Rev. B* **22**, 863 (1980).
- <sup>42</sup>M. Gurioli, A. Vinattieri, M. Colocci, C. Deparis, J. Massies, G. Neu, A. Bosacchi, and S. Franchi, *Phys. Rev. B* **44**, 3115 (1991).
- <sup>43</sup>Y. Narukawa, Y. Kawakami, S. Fujita, and S. Nakamura, *Phys. Rev. B* **59**, 10283 (1999).
- <sup>44</sup>E. Berkowicz, D. Gershoni, G. Bahir, E. Lakin, D. Shilo, E. Zolotoyabko, A. C. Abare, S. P. Denbaars, and L. A. Coldren, *Phys. Rev. B* **61**, 10994 (2000).
- <sup>45</sup>J. Feldman, G. Peter, E. O. Göbel, P. Dawson, K. Moore, C. Foxon, and R. J. Elliott, *Phys. Rev. Lett.* **59**, 2337 (1987).

- <sup>46</sup>L. C. Andreani, F. Tassone, and F. Bassani, *Solid State Commun.* **77**, 641 (1991).
- <sup>47</sup>P. Lefebvre, J. Allegre, B. Gil, A. Kavokine, H. Mathieu, W. Kim, A. Salvador, A. Botchkarev, and H. Morkoc, *Phys. Rev. B* **57**, R9447 (1998).
- <sup>48</sup>S. L. Chuang and C. S. Chang, *Phys. Rev. B* **54**, 2491 (1996); *Semicond. Sci. Technol.* **12**, 252 (1996).
- <sup>49</sup>A. Bykhovski, B. Gelmont, and M. Shur, *J. Appl. Phys.* **74**, 6734 (1993).
- <sup>50</sup>S. Khatsevich, D. H. Rich, X. Zhang, W. Zhou, and P. D. Dapkus, *J. Appl. Phys.* **95**, 1832 (2004).
- <sup>51</sup>H. J. Kim, H. Na, S.-Y. Kwon, H.-C. Seo, H. J. Kim, Y. Shin, K.-H. Lee, Y.-W. Kim, S. Yoon, H. J. Oh, C. Sone, Y. Park, Y.-H. Cho, Y. Sun, and E. Yoon, *Phys. Status Solidi C* **0**, 2834 (2003).
- <sup>52</sup>A. Kunold and P. Pereyra, *J. Appl. Phys.* **93**, 5018 (2003).
- <sup>53</sup>W. Shan, B. D. Little, J. J. Song, Z. C. Feng, M. Shurman, and R. A. Stall, *Appl. Phys. Lett.* **69**, 3315 (1996).
- <sup>54</sup>A. V. Voznyy and V. G. Deibuk, *Semiconductors* **38**, 304 (2004).
- <sup>55</sup>V. Fiorentini, F. Bernardini, F. D. Sala, A. D. Carlo, and P. Lugli, *Phys. Rev. B* **60**, 8849 (1999).
- <sup>56</sup>F. Bernardini and V. Fiorentini, *Phys. Status Solidi B* **216**, 391 (1999).
- <sup>57</sup>M. Leroux, N. Grandjean, J. Massies, B. Gil, P. Lefebvre, and P. Bigenwald, *Phys. Rev. B* **60**, 1496 (1999).
- <sup>58</sup>Ursula M. E. Christmas, A. D. Andreev, and D. A. Faux, *J. Appl. Phys.* **98**, 073522 (2005).
- <sup>59</sup>D. H. Rich, H. T. Lin, and A. Larsson, *J. Appl. Phys.* **77**, 6557 (1995).
- <sup>60</sup>I.-H. Tan, G. L. Snider, L. D. Chang, and E. L. Hu, *J. Appl. Phys.* **68**, 4071 (1990).
- <sup>61</sup>J.-W. Wu, *Solid State Commun.* **69**, 1057 (1989).
- <sup>62</sup>Y. Tang, H. T. Lin, D. H. Rich, P. Colter, and S. M. Vernon, *Phys. Rev. B* **53**, R10501 (1996).
- <sup>63</sup>E. L. Ivchenko and A. V. Kavokin, *Sov. Phys. Semicond.* **25**, 1070 (1991).